PHYSICAL REVIEW B **74**, 104115 (2006)

Neutron scattering studies of short-range order, atomic displacements, and effective pair interactions in a null-matrix $^{62}\mathrm{Ni}_{0.52}\mathrm{Pt}_{0.48}$ crystal

J. A. Rodriguez* and S. C. Moss
Department of Physics, University of Houston, Houston, Texas 77204-5005, USA

J. L. Robertson
Oak Ridge National Laboratory, P.O. Box 2008 MS 6393, Oak Ridge, Tennessee 37831-6393, USA

J. R. D. Copley and D. A. Neumann
National Institute of Standards and Technology, 100 Bureau Drive, MS 8562, Gaithersburg, Maryland 20899-8562, USA

J. Major
Max Planck Institut für Metallforschung, Heisenbergstraße 3, 70569 Stuttgart, Germany

(Received 22 March 2006; revised manuscript received 7 August 2006; published 28 September 2006)

The best known exception to the Heine-Sampson and Bieber-Gauthier arguments for ordering effects in transition metal alloys (similar to the Hume-Rothery rules) is a NiPt alloy, whose phase diagram is similar to that of the CuAu system. Using neutron scattering we have investigated the local atomic order in a null-matrix $^{62}\mathrm{Ni}_{0.52}\mathrm{Pt}_{0.48}$ single crystal. In a null-matrix alloy, the isotopic composition is adjusted so that the average neutron scattering length vanishes (^{62}Ni has a negative scattering length nearly equal in magnitude to that of Pt). Consequently, all contributions to the total scattering depending on the average lattice are suppressed. The only remaining components of the elastic scattering are the short-range order (SRO) and size effect terms. These data permit the extraction of the SRO parameters (concentration-concentration correlations) as well as the displacement parameters (concentration-displacement correlations). Using the Krivoglaz-Clapp-Moss theory, we obtain the effective pair interactions (EPIs) between near neighbors in the alloy. The results can be used by theorists to model the alloy in the context of the electronic theory of alloy phase stability, including a preliminary evaluation of the local species-dependent displacements. Our maps of $V(\mathbf{q})$, the Fourier transform of the EPIs, show very similar shapes in the experimental and reconstructed data. This is of importance when comparing to electronic structure calculations.

DOI: 10.1103/PhysRevB.74.104115 PACS number(s): 61.12.−q, 71.20.Be, 61.82.Bg, 64.60.Cn

I. INTRODUCTION

The NiPt alloy system has been the subject of intensive theoretical investigation for the past two decades for two main reasons. First, it does not follow the Heine-Sampson[1] and Bieber-Gauthier[2] arguments (similar to the Hume-Rothery[3] electron per atom ratio rules) for ordering effects in transition metal alloys. Second, in the NiPt alloy, Pt segregates toward the (100) and (111) topmost surface layers, while there is reversed segregation at the (110) surface, which appears to be nearly completely covered by Ni.[4,5] This phenomenon relates to the alloy's desirable catalytic properties.

There are several theories about the origins of ordering in NiPt alloys. Bieber and Gauthier[2] suggested that magnetic effects were responsible for such behavior, but in NiPt the ferromagnetism decreases very rapidly as the Ni concentration decreases leaving increasingly weak paramagnetism. With a Ni concentration of 50% or more, this magnetization vanishes, and the argument would seem to be considerably weaker. Treglia and Duscastelle[6] indeed found that spin-orbit coupling favors ordering in NiPt, but the magnitude is not sufficient to account for the observed ordering temperatures.

Using the Korringa-Kohn-Rostoker coherent potential approximation electronic-structure methods,[7] Pinski *et al.*[8] found that relativity was not responsible for long-range or short-range order, because relativistic effects predominantly increase *s*-electron cohesion, such that the ordering energy is not significantly affected. Moreover, they found that charge transfer does not play a role because Ni and Pt have similar electronegativities and thus each atom in the alloy remains essentially charge neutral. More importantly, they found that the size disparity between Ni and Pt dictates the relative bandwidths in the average alloy lattice (related to off-diagonal disorder), leading to low-energy t_{2g} hybridization states and a strong ordering tendency due to band-filling of only those new states. In fact, the predicted transition temperature was 632 °C compared to the observed 645 °C. This size-related effect on the electronic structure was argued as the origin of Hume-Rothery's size-effect rule because increasing the "size" fictitiously by increasing the average lattice saw the hybridization states vanish, along with the short-range order.

As such, similar band-filling mechanisms argued by Heine and Sampson[1] are in effect, but are counter to the Bieber and Gauthier[2] argument that size disparity accentuates phase segregation. Lu *et al.*[9] also argue that size plays a dominant role, but, while they claim that *s*-electron cohesion is responsible for ordering, they considered only the formation energy, not the ordering energy. In addition it has been found that relativistic effects in low coordination 5*d* elements reduce the atomic mismatch with respect to the pure

©2006 The American Physical Society

$3d$ elements[10–12] and this was later taken into account by Wang and Zunger[13] to argue that these relativistic effects *reduce* the elastic strain energy.

In this paper we describe a neutron scattering study of short-range order (SRO) and the size-effect (SE) in a NiPt alloy, as well as the effective pairwise interactions (EPIs) that quantify the ordering tendency. In principle, the EPIs can be of purely electronic origin or they can arise from a combination of electronic and strain contributions.[14] In Sec. II we briefly review the diffuse scattering theory applied to a null-matrix alloy and we also discuss the effective pairwise interactions. In Sec. III we describe the sample and the instrument configuration used for this work. Section IV contains a discussion of the resulting numerical values of the structural parameters obtained in the experiment. These include EPIs and important information on the apparent deviation of the NiPt nearest neighbor separation from the value given by the average lattice parameter and Poisson ratio in the ordered state. In Sec. V we briefly discuss neutron scattering measurements on a natural abundance $Ni_{0.52}Pt_{0.48}$ crystal. We conclude with a brief description of further work in progress.

II. DIFFUSE NEUTRON SCATTERING

In general, the total scattering from a binary solid solution can be separated into Bragg scattering which yields information about the average lattice and diffuse scattering associated with local deviations from the average structure. The diffuse scattering can be further divided into a component arising from the SRO which is related to the concentration-concentration correlation function, the SE which is related to the concentration-static displacement correlation function, and the quadratic diffuse scattering (QDS) which is composed of time-dependent (inelastic) and time-averaged (elastic) terms, and refers to both the thermal (TDS) and higher order terms that arise when the diffuse intensity is expanded in terms of the static displacements. An elegant discussion of the relationship between the various correlations and the components of the diffuse intensity can be found in Dietrich and Fenzl[15,16] and in Reinhard *et al.*[17] The expression for the total intensity can be written as

$$I_{Total} = I_{Bragg} + I_{SRO} + I_{SE} + I_{QDS}. \tag{1}$$

In the present study the experiment is designed to isolate the SRO and SE components of the diffuse scattering which will be analyzed to determine the local atomic environments as well as the EPIs. In order to minimize contributions from the average lattice (Bragg) scattering and QDS and at the same time enhance the SRO and SE scattering, we chose an alloy very near the null-matrix composition. The single crystal was made from the isotope ^{62}Ni (scattering length $b_{^{62}\mathrm{Ni}}=-8.7$ fm) and Pt (scattering length $b_{\mathrm{Pt}}=9.6$ fm) ($1\ \mathrm{fm}=1\times10^{-15}$ m), with respective concentrations $c_{^{62}\mathrm{Ni}}=0.52$ and $c_{\mathrm{Pt}}=0.48$, i.e., chemical composition $^{62}Ni_{0.52}Pt_{0.48}$, such that the mean scattering length $\langle b\rangle=(c_{\mathrm{Ni}}b_{\mathrm{Ni}}+c_{\mathrm{Pt}}b_{\mathrm{Pt}})=0.08$ fm was extremely small (ideally zero) as compared to the scattering contrast $\delta b=|b_{\mathrm{Ni}}-b_{\mathrm{Pt}}|=18.3$ fm; Bragg scattering and dominant terms of the QDS are proportional to the square of the mean scattering length, whereas the SE and SRO scattering depend on powers of the contrast. For a crystal with the same chemical composition made with natural nickel ($b_{\mathrm{Ni}}=10.3$ fm), $\langle b\rangle$ is 9.96 fm and δb is 0.7 fm. Thus the SRO intensity per atom is about 700 times larger for the isotopic crystal than for the natural crystal. Furthermore the ratio $\delta b/\langle b\rangle$ is 218 for the isotopic crystal, 0.07 for the natural crystal, and 0.96 for x rays (using atomic numbers instead of scattering lengths). These numbers suggest that an x-ray experiment might reveal useful information but the beauty of the null-matrix method with neutrons is that the diffuse scattering can be measured very close to Bragg points because the Bragg peak intensity is essentially zero. The remaining components of the inelastic scattering not suppressed at the null-matrix composition were eliminated using the time-of-flight technique described in Sec. III. Thus the expression for the total scattering can be reduced to

$$I_{Total} = I_{SRO} + I_{SE}. \tag{2}$$

The null-matrix technique was first used by Mozer *et al.*[18] followed by Vrijen and Radelaar,[19] and Wagner *et al.*[20] with CuNi powder samples. This is, to our knowledge, the first use of the null-matrix technique to study a single crystal alloy.

The SRO component of the diffuse intensity, I_{SRO}, yields information about the distribution of atoms on the lattice sites. Consider a sample that consists of two types of atoms, A and B, randomly located on a crystal lattice. The atomic concentrations are c_A and c_B ($c_A+c_B=1$), and the total number of atoms is N. In this case I_{SRO} is given by the Laue monotonic scattering expression[21,22]

$$I_{SRO} = I_{Laue} = Nc_Ac_B(b_A-b_B)^2, \tag{3}$$

where b_A and b_B are the neutron scattering lengths of A and B atoms. If we introduce local concentration correlations,[21–27] the distribution of atoms will not be completely random. For example, given a random distribution the probability of finding a B atom as the nearest neighbor of an A atom is simply c_B. However, if there is a preference for A atoms to have B atoms as their first neighbors, the probability of finding a B atom as the first neighbor of an A atom is greater than c_B. Concentration correlations modulate the Laue intensity given in Eq. (3) and can be expressed in terms of Fourier components such that for a cubic lattice the intensity is given by[21,22]

$$I_{SRO} = Nc_Ac_B(b_A-b_B)^2\sum_n \alpha(n)\sum_{k=1}^{m(n)} e^{i\mathbf{Q}\cdot\mathbf{r}(nk)}. \tag{4}$$

In this expression $\mathbf{Q}$ is the scattering vector, $\mathbf{r}(nk)$ connects an arbitrary (A or B) atom at the origin to the kth atom in the nth shell of neighbors, and $m(n)$ denotes the number of atoms in that shell. (Neighbors at the same distance from the origin but with different symmetry have different shell indices.) The Warren-Cowley SRO parameters[21,22] are directly defined in terms of the occupation probabilities, as follows:

$$\alpha(n) = 1 - \frac{p_A(n)}{c_A} = 1 - \frac{p_B(n)}{c_B}, \tag{5}$$

where $p_A(n)$ is the probability of finding an atom of type A in the nth shell of neighbors surrounding an atom of type B and $p_B(n)$ is the probability of finding an atom of type B in the nth shell of neighbors surrounding an atom of type A. For the random distribution $\alpha(0)=1$ and $\alpha(n)=0$ for $n>0$. Substituting into Eq. (4) we recover Eq. (3).

The SE scattering is associated with the mean interatomic displacements.[23] If $r(n)$ is the mean distance between an atom at the origin and its neighbor in the nth shell, and r^n_{AA} is the corresponding mean distance for atoms of type A, with similar definitions for r^n_{AB} and r^n_{BB}, we introduce fractional displacements ϵ^n_{AA}, ϵ^n_{AB}, and ϵ^n_{BB} as follows:

$$r^n_{AA} = r(n)(1+\epsilon^n_{AA}), \quad r^n_{AB} = r(n)(1+\epsilon^n_{AB}),$$

$$r^n_{BB} = r(n)(1+\epsilon^n_{BB}). \tag{6}$$

The general expression for the size-effect intensity, developed by Borie,[28,29] is then given by

$$I_{SE} = I_{Laue}\sum_n \gamma(n)\sum_{k=1}^{m(n)} i\mathbf{Q}\cdot\mathbf{r}(nk)e^{i\mathbf{Q}\cdot\mathbf{r}(nk)}, \tag{7}$$

where the size-effect parameter for the nth shell is

$$\gamma(n) = \left(\frac{1}{b_B - b_A}\right)\left[-b_A\left(\frac{c_A}{c_B}+\alpha(n)\right)\epsilon^n_{AA} + b_B\left(\frac{c_B}{c_A}+\alpha(n)\right)\epsilon^n_{BB}\right]. \tag{8}$$

For *each* shell the average lattice distance must be equal to the weighted average of the separate interatomic distances. It follows that

$$\epsilon^{\mathrm{n}}_{\mathrm{AB}} = -\frac{1}{2}\left[\frac{\frac{c_A}{c_B}+\alpha(n)}{1-\alpha(n)}\epsilon^n_{AA} + \frac{\frac{c_B}{c_A}+\alpha(n)}{1-\alpha(n)}\epsilon^n_{BB}\right]. \tag{9}$$

It is important to note that in Borie's treatment $r(n)$, ϵ and γ are vectors whose Cartesian components can be retrieved from the data once we have completed an additional experiment, namely x-ray scattering from a normal $\mathrm{Ni}_{0.52}\mathrm{Pt}_{0.48}$ crystal collecting data throughout a symmetry volume. This study is underway, using a flat extended-face crystal prepared in Jülich, Germany. In Eqs. (6)–(9) we only consider the radial components of $r(n)$, ϵ and γ. This is not a severe simplification for cubic crystals though there can be significant deviations in crystals with selected soft modes, but that is not the case here. For a complete discussion of these matters, and of the equivalence of the Dietrich-Fenzl and Borie theories with regard to the SRO, SE, and QDS parameters that can generally be extracted from diffuse scattering data (of course, including the null-matrix case), we refer the reader to the original papers[15,16,28,29] and to Reinhard *et al.*[17]

The SRO and SE intensities are also modified by the thermal vibration of the atoms through a Debye-Waller factor (DWF),[30] e^{-M}. The DWF is a function of $|\mathbf{Q}|$ and of the shell index n because near neighbors experience smaller relative displacements than distant neighbors. Introducing separate DWFs for each type of atom we rewrite Eqs. (4) and (7) as

$$I_{SRO} + I_{SE} = Nc_Ac_B\sum_n (b_Ae^{-M_A} - b_Be^{-M_B})^2 \times \sum_{k=1}^{m(n)} [\alpha(n) + \gamma(n)i\mathbf{Q}\cdot\mathbf{r}(nk)]e^{i\mathbf{Q}\cdot\mathbf{r}(nk)}. \tag{10}$$

The SRO is directly related to the EPIs. Using the SRO, especially above a first-order transition such as ours, these EPIs can be evaluated using a mean field representation,[31–35] where the Ising-like Hamiltonian is written as

$$H = \frac{1}{2}\sum_{jj'}[V^{AA}_{jj'}\sigma^A_j\sigma^A_{j'} + V^{BB}_{jj'}\sigma^B_j\sigma^B_{j'} + V^{AB}_{jj'}(\sigma^A_j\sigma^B_{j'} + \sigma^B_j\sigma^A_{j'})]. \tag{11}$$

If an atom of type A is on site j the projection operators $\sigma^A_j=1$ and $\sigma^B_j=0$. If an atom of type B is on site j, $\sigma^A_j=0$ and $\sigma^B_j=1$. Note that while this is a traditional Ising Hamiltonian, several neighbors contribute and the EPIs have separate values for each shell. Using the Flinn[36] operators (known as spin-deviation operators in magnetism),

$$\bar{\sigma}_j = 2(\sigma^A_j - c_A) \equiv 2(c_B - \sigma^B_j), \tag{12}$$

Eq. (11) yields:

$$H = \frac{1}{4}\sum_{jj'} V_{jj'}\bar{\sigma}_j\bar{\sigma}_{j'}, \tag{13}$$

with

$$V_{jj'} = \tfrac{1}{2}(V^{AA}_{jj'} + V^{BB}_{jj'} - 2V^{AB}_{jj'}). \tag{14}$$

The $V_{jj'}$ are analogous to the exchange interactions in an Ising magnet: $V_{jj'}>0$ denotes ordering (antiferromagnetism), whereas $V_{jj'}<0$ denotes clustering (ferromagnetism). Representing the EPIs, they are concentration and temperature dependent due to the varying atomic arrangements between j and j'.[37] The sums over j and j' can be replaced by a sum over the vectors $\mathbf{r}(nk)$ that connect an arbitrary origin atom to its neighbors. We shall henceforth use this simplified notation.

There are many methods to obtain the EPIs from the SRO parameters. The most commonly used are the inverse Monte Carlo (IMC) method,[24,37,38] which finds the V's that are consistent with the simulated structure using *occupational probabilities*;[39] the Krivoglaz-Clapp-Moss (KCM) approximation[31–34] which uses a mean-field approach to determine the EPIs; and the γ-expansion method (GEM), developed by Masanskii (now Tsatskis), Tokar *et al.*,[40] which is an extension of the KCM approximation in the spirit of the spherical model, and assumes that the pair correlation function falls off exponentially with the interatomic distance $r(n)$, giving these methods similar results.[35] We will use the KCM and its extension (GEM). Using Eq. (4) we define the intensity $I(\mathbf{q})$ as before, but now in units of the Laue intensity [Eq. (3)]; $\mathbf{q}=\mathbf{Q}-\mathbf{G}$ is a wave vector of the fluctuation spectrum, $\mathbf{Q}$ is the scattering vector, and $\mathbf{G}$ is a reciprocal lattice vector. The intensity is

$$I(\mathbf{q}) = \sum_{nk} \alpha(n) e^{i\mathbf{q}\cdot\mathbf{r}(nk)}, \tag{15}$$

and the Fourier transform of the EPI is

$$V(\mathbf{q}) = \sum_{nk} V(n) e^{i\mathbf{q}\cdot\mathbf{r}(nk)}. \tag{16}$$

Krivoglaz,[31] and Clapp and Moss[32] independently related these equations writing

$$I^{KCM}(\mathbf{q}) = \frac{1}{1 + 2c_A c_B \beta V(\mathbf{q})}, \tag{17}$$

where $\beta = (k_B T)^{-1}$. [Originally Clapp and Moss used a different numerator obtained from the condition that the integral of the diffuse scattering over a Brillouin zone must be a constant, namely 1.00 in Laue units. Another normalization procedure used the condition $\alpha(0) = 1.00$. Krivoglaz derived the expression in Eq. (17).] For cubic lattices, Masanskii *et al.*[40] obtained the following GEM result in terms of the approximate KCM result:

$$V^{GEM}(n) = V^{KCM}(n) + \frac{1}{2\beta}\Sigma_n, \tag{18}$$

with

$$\Sigma_1 = A\alpha(1)^2 + B\alpha(1)^3; \quad \Sigma_{2,3} = A\alpha(2,3)^2;$$

$$\Sigma_n = 0 \quad (n > 3), \tag{19}$$

where

$$A = \frac{(1 - 2c_A)^2}{2c_A^2 c_B^2}; \quad B = \frac{(1 - 6c_A c_B)^2 - 3(1 - 2c_A)^4}{6c_A^3 c_B^3}. \tag{20}$$

III. EXPERIMENTAL ISSUES

The $^{62}\mathrm{Ni}_{0.52}\mathrm{Pt}_{0.48}$ single crystal was grown at the Max-Planck-Institut für Metallforschung-Stuttgart. Grown as a cylinder with a diameter of 4 mm and a length of 15 mm, it shows a homogeneous degree of perfection with a local mosaicity better than 0.2°, measured using a 660 keV gamma diffractometer. The thermal treatment of the crystal involved extended anneals from 1350 °C, slowly decreasing to 700 °C, and then quenching into ice water to maintain the disordered phase.

In a scattering experiment the shapes of the diffuse peaks are mainly determined by the occupational probabilities of the atoms, i.e., the SRO (for the moment ignoring the anomalously small asymmetric SE scattering as compared with alloys with size disparities similar to that of NiPt, such as CuAu[41]). Since these probabilities are temperature dependent we can determine the equivalent temperature from which the sample was quenched (the "fictive" temperature) by examining the shapes of the diffuse peaks at different temperatures. To this end we performed at-temperature scans at the high flux isotope reactor (HFIR), Oak Ridge National Laboratory, using the HB-3 triple axis spectrometer and a high temperature furnace. The objective was to find the temperature at which the width of the (001) diffuse peak matched that of the diffuse peak measured with the sample quenched to room temperature. Measurements were made at 1000 °C, 900 °C, 800 °C, 700 °C, 675 °C, 660 °C, 655 °C, and 25 °C. At each temperature the (001) diffuse

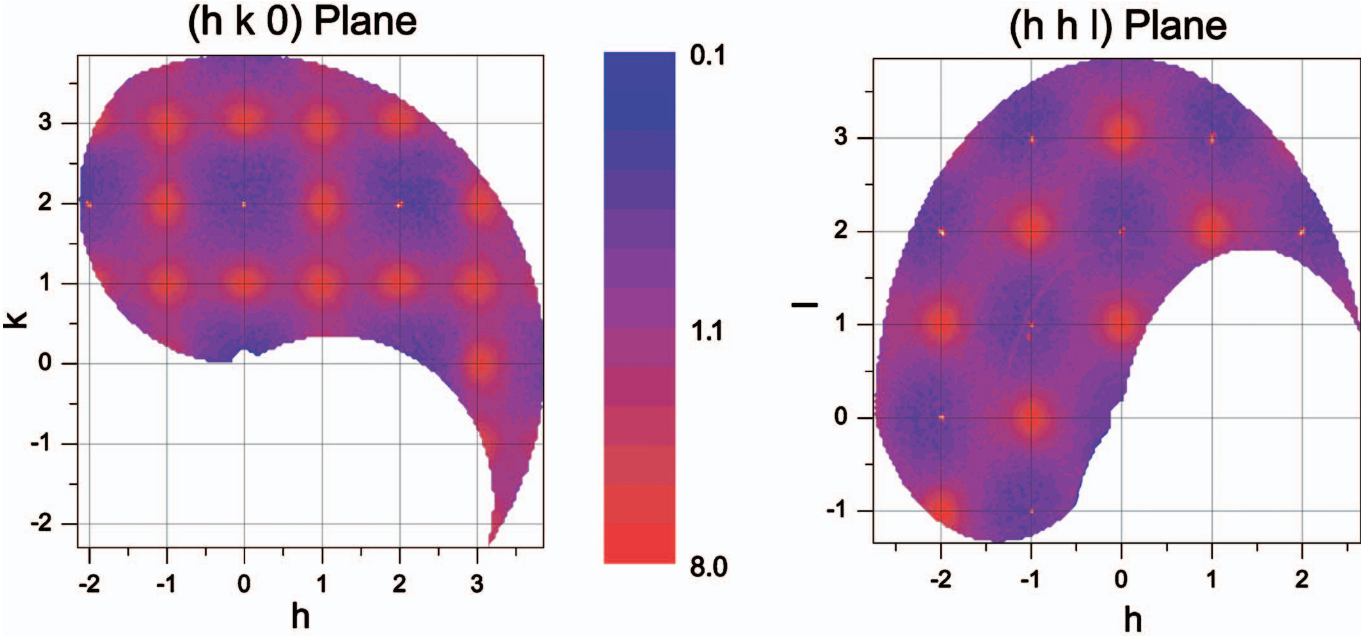

FIG. 1. (Color) $^{62}\mathrm{Ni}_{0.52}\mathrm{Pt}_{0.48}$ experimental maps of the diffuse scattering intensity. The intensity scale is logarithmic. The tiny dots are the very weak Bragg reflections. In the right-hand plot, very weak powder scattering from the sample post is evident. With respect to the Bragg dots in the (*hhl*) plane we clearly see the SE-induced shifts of the diffuse peaks.

TABLE I. $^{62}Ni_{0.52}Pt_{0.48}$ SRO parameters. Note that the following groups of shells have the same radius: (9,10), (14,15), (18,19), (20,21), (22,23), (29–31), (33–35).

Shell number n	Shell index lmn	$\alpha(n)$
0	000	1.022(23)
1	110	−0.114(4)
2	200	0.117(6)
3	211	−0.012(4)
4	220	0.069(4)
5	310	−0.017(3)
6	222	0.038(3)
7	321	−0.015(3)
8	400	0.010(6)
9	330	−0.015(4)
10	411	−0.007(4)
11	420	0.029(4)
12	332	−0.005(1)
13	422	0.015(3)
14	510	0.002(4)
15	431	0.000(3)
16	521	−0.010(4)
17	440	0.003(4)
18	530	−0.003(3)
19	433	−0.002(3)
20	600	−0.013(8)
21	442	−0.001(4)
22	611	0.004(3)
23	532	0.001(3)
24	620	0.010(3)
25	541	0.001(3)
26	622	0.004(3)
27	631	−0.005(3)
28	444	0.018(8)
29	710	−0.002(3)
30	550	−0.010(6)
31	543	−0.006(3)
32	640	0.010(3)
33	721	−0.001(0)
34	552	0.005(3)
35	633	0.005(4)

peak was fitted using a Voigt function. From a plot of the width of the peak as a function of temperature we obtained a fictive temperature of 679 °C for the quenched crystal. (The equilibrium ordering temperature is ~645 °C.)

The neutron scattering measurements were performed using the disk chopper spectrometer (DCS) at the National Institute of Standards and Technology's Center for Neutron Research (NCNR). The DCS is a multichopper time of flight spectrometer that is mostly used for studies of low-energy excitations and diffusive motions in materials.[42,43] The choppers deliver monochromatic pulses of neutrons to the sample and the times of flight of the scattered neutrons are used to calculate energy transfers knowing the sample-detector distance which is 4010 mm, common to all detectors. From the scattering angle and the orientation of the sample with respect to the incident and scattered beams, the wave vector transfer $\mathbf{Q}$ can also be calculated. Since the desired diffuse scattering is elastic, the intensity in any given detector was obtained by summing the counts over time channels either side of (and including) the elastic time channel and within the experimentally determined range of the instrumental resolution function.

The DCS detectors are arranged in three banks with their centers located above, below, and in the scattering plane. To simplify the correction for vertical resolution, we only included the 325 detectors in the middle bank. Scattering angles for this bank range from −30° to −5° and from 5° to 140°. Since the height of the detectors is considerable (400 mm) the vertical resolution at each $|\mathbf{Q}|$ must be taken into account.

A critical aspect of the diffuse scattering data analysis requires conversion of the raw intensity into appropriate units and correcting the data for vertical resolution in order to obtain and interpret the SRO and SE structural parameters in a plane of reciprocal space. The complexity of the corrections depends on the accuracy required. We will describe our vertical integrated diffuse intensity calculations using a finite element method and corrections for sample absorption in a future publication. A standard vanadium normalization was used to express raw intensities in Laue units [Eq. (3)].

The sample was glued to an aluminum post coated with neutron-absorbing Gd_2O_3 paint, and mounted within an evacuated aluminum vessel to minimize air scattering. An oscillating radial collimator was used to reduce scattering from the vessel. Room temperature data were collected in the $[001]$ and $[1\bar{1}0]$ [i.e., the $(hk0)$ and (hhl)] scattering planes using a wavelength of 1.8 Å. In each case, having first aligned the sample, data were collected for a series of crystal orientations in steps of 1°, more than sufficient to cover the requisite range in angles (which depends on the scattering plane). Typical counting times were of order 30 min per crystal orientation.

IV. RESULTS

Normalized elastic scattering intensities are shown in Fig. 1. As expected there is no evidence of QDS intensity. The Bragg peaks from normal NiPt are several orders of magnitude larger than the diffuse scattering but there are no Bragg peaks in a null-matrix crystal. A small deviation in the composition of our crystal from the null-matrix condition produces very small Bragg peaks (which are useful for alignment purposes). We clearly see the SRO diffuse peaks, asymmetrically modulated due to the SE scattering.

Using singular value decomposition[44] and Eq. (10), with DWFs computed from the mean displacements that result from our fits, $\langle u_{\mathrm{Ni}}^2\rangle = 0.00369$ Å^2 and $\langle u_{\mathrm{Pt}}^2\rangle = 0.00395$ Å^2, we fitted 35 SRO parameters and 15 SE parameters. The values of $\langle u_{\mathrm{Ni}}^2\rangle$ and $\langle u_{\mathrm{Pt}}^2\rangle$ are nearly equal and therefore close to the mean value for $Ni_{0.52}Pt_{0.48}$. Their effect on the SRO and SE

TABLE II. $^{62}Ni_{0.52}Pt_{0.48}$ SE parameters. See the caption to Table I.

Shell number *n*	Shell index *lmn*	$\gamma(n)$
1	110	0.00532(26)
2	200	−0.00129(6)
3	211	−0.00098(3)
4	220	−0.00022(1)
5	310	0.00046(2)
6	222	−0.00007(0)
7	321	0.00008(0)
8	400	−0.00023(1)
9	330	0.00022(1)
10	411	−0.00013(0)
11	420	−0.00005(0)
12	332	0.00007(0)
13	422	−0.00004(0)
14	510	0.00008(0)
15	413	−0.00002(0)

parameters is small. For the data analysis we chose the real-space least-squares method over other treatments (e.g., Borie,[45] Dietrich and Fenzl,[15,16] or Krivoglaz[31]) because least squares allow us to take into account statistical errors and correlations between the SRO and SE parameters. The **Q**-space analysis of Krivoglaz,[31] while more transparent to view in terms of SRO, SE, and QDS, is also (currently) unable to retrieve the separate species-dependent displacements in the SE and is not applicable to our null-matrix condition. The least-squares method also permits the use of a more limited range of **Q** space. The reconstructed data are essentially identical to the experimental data (Fig. 1). The error bars were calculated using the correlation matrix obtained with the SVD algorithm.[44]

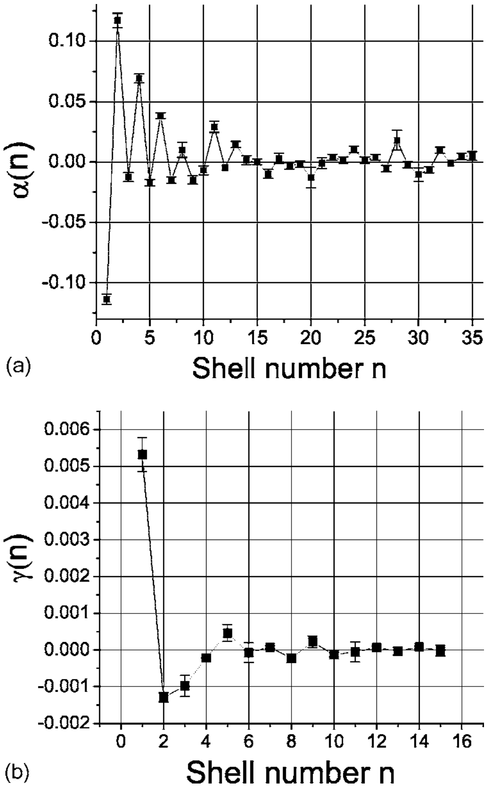

FIG. 2. $^{62}Ni_{0.52}Pt_{0.48}$ SRO and SE parameters. The SRO parameters $\alpha(n)$ oscillate about zero, indicating a tendency toward ordering for the first several neighbors. The SE parameters $\gamma(n)$ vanish quickly beyond the fifth neighbor shell. See the caption to Table I.

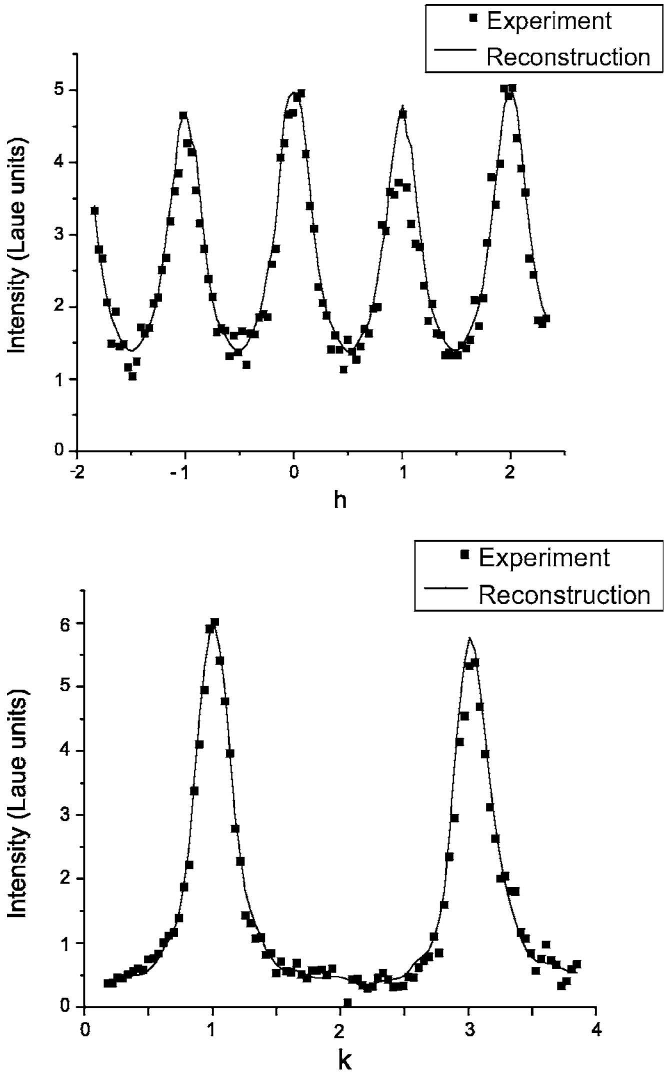

FIG. 3. $^{62}Ni_{0.52}Pt_{0.48}$ reconstructed and experimental line scans, shown as solid lines and points, respectively, along the $\langle h\,3.1\,0\rangle$ (upper panel) and $\langle 0\,k\,0\rangle$ (lower panel) directions. One can clearly see the asymmetric SE addition to the symmetric diffuse SRO peaks.

The SRO parameters [Table I and Fig. 2(a)] reveal a tendency to ordering. Negative SRO parameters mean a preference for "unlike" neighbors whereas positive values indicate a preference for "like" neighbors. Alternating negative and positive values mean that there is preference to ordering. The 0th SRO parameter, $\alpha(0)$, is 1.02, close to 1.00 which is required but rarely obtained. This result represents an excellent check on our removal of extraneous scattering and on our normalization procedure. As the shell number n in-

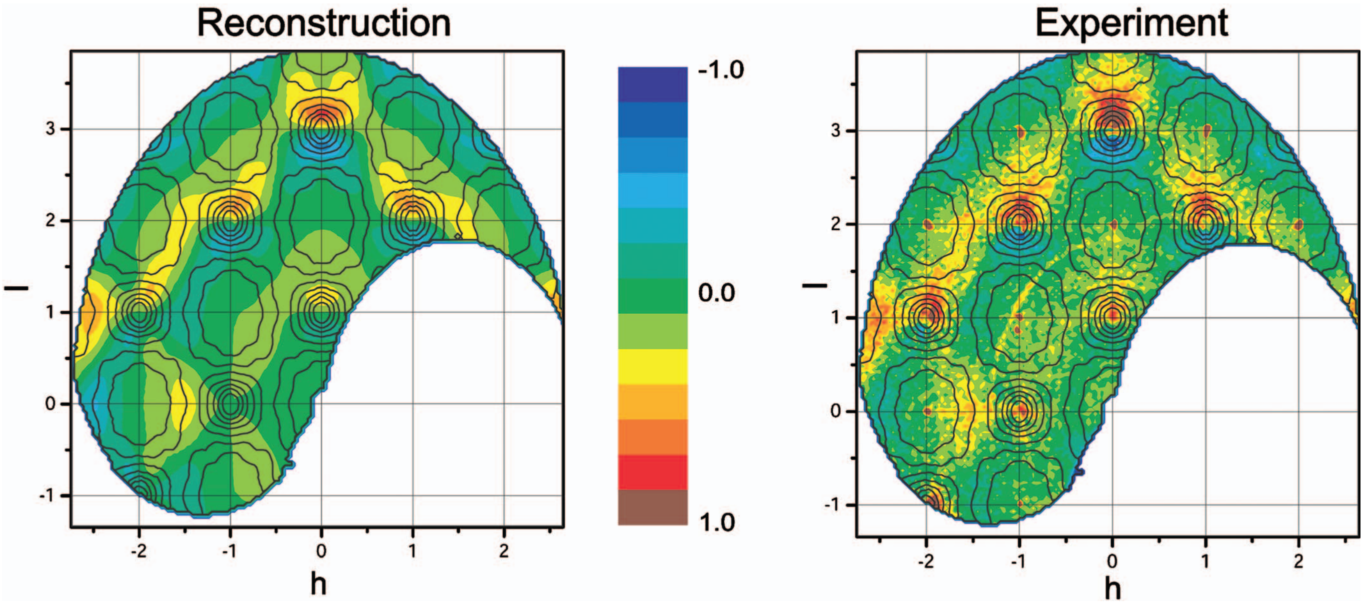

FIG. 4. (Color) Reconstructed and experimental data for $^{62}Ni_{0.52}Pt_{0.48}$ in the $[1\bar{1}0]$ plane, i.e., the (hhl) plane. The SE intensity, expressed in Laue units, is plotted on a linear scale. The SE parameters were experimentally obtained and then used to create the reconstructed data. The experimental data were obtained by subtracting the SRO scattering (presented as solid black contours) from the original data. The SRO maximum intensity is about six times the SE maximum intensity, revealing the SE scattering as an asymmetric "modulation" of the SRO peaks. The partial (yellow) ring in the experimental data comes from the Al post holding the crystal.

creases, the SRO parameters decrease and the probability of finding a neighboring atom becomes essentially equal to the random value given by the composition; i.e., the intensity is given by the Laue expression for the more distant shells. It is perhaps interesting that several values of $\alpha(n)$ are larger in magnitude than expected. For example $\alpha(16)$ and $\alpha(28)$ are well outside the error bars but we do not have any explanation for these features and we cannot eliminate the possibility that errors originating with detector length have not been completely corrected. The correlation length was estimated from the radial diffuse peak width at half-height, which gave a value of 5.83 Å, equivalent to 1.58 lattice constants.

The SE parameters [Table II and Fig. 2(b)] are large for the first three neighbors but decay faster than the SRO parameters. The SE scattering modulates the SRO scattering, producing asymmetric diffuse peaks as shown in Fig. 3. It is not possible to extract individual Ni-Ni, Ni-Pt, and Pt-Pt displacements from the SE parameters, but linear combinations can be obtained using Eqs. (8) and (9). For nearest neighbor sites we obtain $0.005\,32=0.461\epsilon_{\text{Ni-Ni}}+0.424\epsilon_{\text{Pt-Pt}}$ and $\epsilon_{\text{Ni-Pt}}=-0.435\epsilon_{\text{Ni-Ni}}-0.363\epsilon_{\text{Pt-Pt}}$, respectively. In their study of $Ni_{0.89}Cr_{0.11}$, Schweika and Haubold[37] were able to extract the Ni-Ni displacement parameter because the ratio of the $\epsilon_{\text{Ni-Ni}}$ and $\epsilon_{\text{Cr-Cr}}$ weight factors was large, ~25, and they could, therefore, neglect $\epsilon_{\text{Cr-Cr}}$. In our case the $\epsilon_{\text{Ni-Ni}}$ and $\epsilon_{\text{Pt-Pt}}$ weight factors are almost identical and we cannot use an analogous approach. If the size disparity between Ni and Pt dominates the tendency to ordering as Pinski *et al.*[8] suggest, and arguing that $\epsilon_{\text{Pt-Pt}}$ is positive and $\epsilon_{\text{Ni-Ni}}$ negative because a Pt atom is about 11% larger than a Ni atom, we find that $\epsilon_{\text{Pt-Pt}}>0.0125$. The $L1_0$ ordered phase consists of alternating planes of Ni and Pt. The c/a ratio is 0.94 which means that the nearest neighbor Ni-Pt distance is smaller than the nearest neighbor distance between like atoms (within the planes). Hence, if the short-range order in our NiPt solid solution tends toward the ordered phase one might expect that the Ni-Ni and Pt-Pt nearest neighbor displacements would both be positive and the Ni-Pt nearest neighbor displacement would be negative. A solution for the disordered phase, similar to that of the ordered phase, is possible, but this would require that $\epsilon_{\text{Ni-Ni}}$ be positive even though the size effect dominates the tendency to ordering. Our x-ray study of a flat extended-face normal $Ni_{0.52}Pt_{0.48}$ crystal should resolve the situation.

The SE intensity, shown in Fig. 4, peaks at a larger **Q** than the SRO, whose diffuse peaks it modulates, and goes below the Laue value near the Bragg peak. This is mainly due to the positive value of the measured $\gamma(1)$ and the negative value of

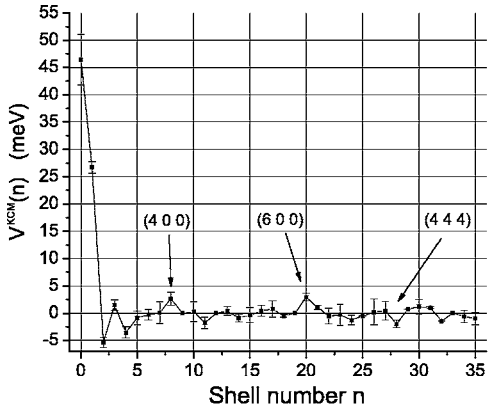

FIG. 5. $^{62}Ni_{0.52}Pt_{0.48}$ EPIs obtained using the KCM theory. Note the enhanced values at (400), (600), and (444) (which is negative). See the caption to Table I.

TABLE III. $^{62}\mathrm{Ni}_{0.52}\mathrm{Pt}_{0.48}$ effective pair interaction potentials (EPIs), using the KCM theory. The values of $V(l\,0\,0)$, underlined, appear to be consistently larger than simple monotonic decay would suggest. See the caption to Table I.

Shell number n	Shell index lmn	V^{KCM} (meV)
0	000	46.42(463)
1	110	26.66(105)
2	200	$\underline{-5.32(92)}$
3	211	1.49(99)
4	220	−3.54(0)
5	310	−0.84(125)
6	222	−0.28(93)
7	321	0.12(99)
8	400	$\underline{2.65(117)}$
9	330	0.00(0)
10	411	0.26(180)
11	420	−1.75(104)
12	332	0.03(0)
13	422	0.39(81)
14	510	−0.82(74)
15	413	−0.33(139)
16	521	0.43(102)
17	440	0.79(149)
18	530	−0.49(028)
19	433	0.03(0)
20	600	$\underline{2.97(70)}$
21	442	1.09(39)
22	611	−0.51(148)
23	532	−0.28(192)
24	620	−1.24(89)
25	541	−0.47(0)
26	622	0.20(238)
27	631	0.47(168)
28	444	−1.98(69)
29	710	0.74(0)
30	550	1.23(133)
31	543	1.04(19)
32	640	−1.43(2)
33	721	0.06(0)
34	552	−0.60(109)
35	633	−0.99(110)

TABLE IV. $^{62}\mathrm{Ni}_{0.52}\mathrm{Pt}_{0.48}$ effective pair interaction potentials (EPIs), using the KCM theory and the KCM theory with the GEM correction.

Shell number n	Shell index lmn	V^{KCM} (meV)	V^{GEM} (meV)
1	110	26.66(105)	26.55(115)
2	200	−5.32(92)	−5.31(93)
3	211	1.49(99)	1.49(99)

$\alpha(1)$. Figure 4 reflects this fact since the SRO contribution has been subtracted.

Using the SRO parameters from Table I, we calculated the EPIs using the KCM method (Fig. 5 and Table III), and using the GEM method for the first three neighbors (Table IV). The largest interactions are given by the first four neighbors and the ordering condition $[V(1)>1$ meV, $V(2)<1$ meV$]$ lies within the stability regime for $L1_0$ in the diagram of $V(1)$ vs $V(2)$.[33] The $L1_0$ structure below T_C is therefore satisfied. $V(0)$ can be understood as a self-energy, as described by Masanskii *et al.*[40] The difference between the two methods is small because the concentration is near 50%. The KCM method requires that $|\alpha(n)| \ll 1$ and $|V(n)| \ll k_BT$ and in this case, where the fictive temperature $k_BT=58.51$ meV, we can expect a slight departure for $V(1)$ from the exact value.

Reinhard and Moss[35] have shown that near the equiatomic composition ($c=0.50$), the KCM method is a very good approximation for the EPIs when compared with the "exact" IMC method; furthermore the GEM extension, namely the correction using Eq. (18), is almost zero for this concentration, giving values nearly identical to the KCM values. An interesting observation, clearly evident in Table III, is that in the $\langle 100 \rangle$ direction $V(n)$ is large as compared with neighboring values. This is not surprising, given the shape of the SRO contours in Fig. 1 in the $[1\bar{1}0]$ plane; $V(28)$ is also anomalous as is $\alpha(28)$. In Fig. 6 we present reconstructed and experimental maps of $V(\mathbf{q})$ in the $[001]$ plane. Clearly $I(\mathbf{q})$ is very weak at the Bragg points where $V(\mathbf{q})$ peaks but these maps are nonetheless quite similar, and provide important information for theoretical purposes. The apparent weak lobes in the $\langle 110 \rangle$ direction are clearly not in the experimental data which represents the total $I(\mathbf{q})$ minus the reconstructed SE intensity.

From a metallurgical point of view, the atom size disparity (called "size effect" by Pinski *et al.*,[8] but not to be confused with its manifestation in the diffuse scattering) can be related to its direct effect on electronic structure and ordering, and thereby to strain energy. In a "ball and spring" system, the strain energy yields a tendency toward unlike nearest neighbors (ordering), based solely on minimizing packing, which does not include any electronic effects. More generally, the effects of atom "size" on the electronic structure can either lead to ordering or to phase segregation.[46] In this case, the atom size disparity is reflected in our data by the small asymmetry due to direct SE scattering and to the same $\langle u^2 \rangle$ for both Ni and Pt. NiPt orders, in agreement with Pinski and co-workers.[47,48]

V. THE NATURAL ABUNDANCE CRYSTAL

Scattering in the $[001]$ and $[1\bar{1}0]$ planes of a natural abundance $\mathrm{Ni}_{0.52}\mathrm{Pt}_{0.48}$ crystal has also been studied using the DCS. The scattering map for the $[1\bar{1}0]$ plane (Fig. 7) is dominated by Bragg scattering and Huang diffuse scattering (HDS). The scattering contrast is very small so that SRO and SE scattering are essentially absent, as discussed in Sec. II.

The HDS is due to the asymptotic displacement field arising from an atom of a different size in its host[28,29,31,49,50] and

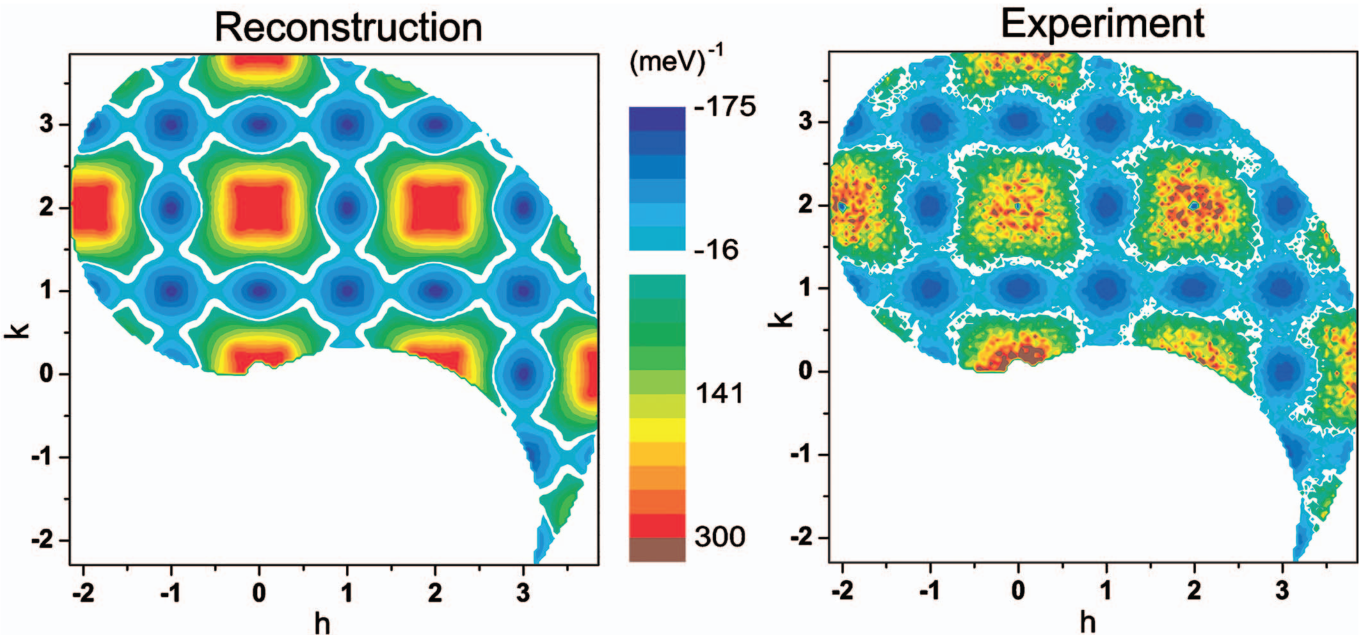

FIG. 6. (Color) ^{62}Ni$_{0.52}$Pt$_{0.48}$ $V(\mathbf{q})$ reconstructed and experimental data for the [001] plane, i.e., the $(hk0)$ plane. The experimental data were obtained by subtracting the SE scattering from the original data, and then using Eq. (17). What appear to be weak $\langle 110\rangle$ lobes in the reconstructed data are simply not present in the experimental map.

corresponds to the dominant elastic term of the QDS discussed in Sec. II. When such a solute atom is present in an otherwise pure crystal, it causes the surrounding atoms to be displaced from their average lattice positions defined by the lattice parameter(s), and the far-field or asymptotic value of this intensity appears in the immediate vicinity of the Bragg peaks, falling off as q^{-2} as does the TDS. The HDS, strictly valid for $c_A \ll 1$, is given by

$$I_{HDS}(\mathbf{Q}) \sim |c_A b_A + c_B b_B|^2 |\mathbf{G}\cdot\tilde{\mathbf{t}}(\mathbf{q})|^2, \qquad (21)$$

where $\tilde{\mathbf{t}}(\mathbf{q})$ is the Fourier transform of the displacement field. The HDS is thus proportional to the number of solute atoms. In concentrated alloys, such as ours, this formalism still applies due to the linear superposition of the displacement fields. Unlike the SRO and SE, the HDS is clearly proportional to the square of the mean lattice scattering as is the one-phonon TDS;[22,51] it is ~ 0 for the null-matrix composition.

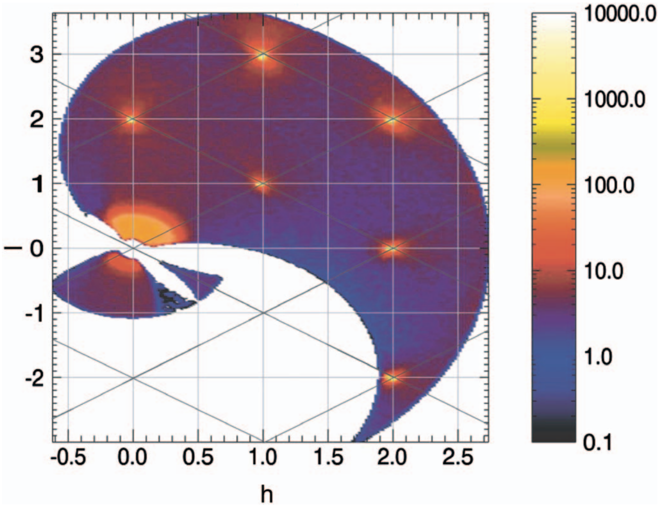

FIG. 7. (Color) Experimental data for the natural abundance Ni$_{0.52}$Pt$_{0.48}$ crystal in the $[1\bar{1}0]$ plane, i.e., the (hhl) plane. The scale is logarithmic, in arbitrary units. The SRO and SE are almost zero and the TDS was removed in the normal way. Only the Bragg scattering and HDS remain. The HDS $[\propto|\mathbf{G}\cdot\tilde{\mathbf{t}}(\mathbf{q})|^2]$ is clearly enhanced in certain directions.

The HDS shows a preferential orientation close to the $\langle 111\rangle$ direction for the (002) and (113) peaks, and to the $\langle 110\rangle$ direction for the (220) peak. The Huang scattering analysis requires considerable effort in order to evaluate the elastic dipole tensor matrix (the Kanzaki forces), given the elastic constants or response function of the crystal. Nonetheless, Fig. 7 indicates a somewhat softer longitudinal elastic response along $\langle 110\rangle$ and related responses given by $|\mathbf{G}\cdot\tilde{\mathbf{t}}(\mathbf{q})|^2$ along other directions: i.e., transverse softness in $\langle 111\rangle$ directions at the (111), (113), (002), and (222) peaks. Work is required on this aspect of our measurements, and this is in progress.

VI. CONCLUSIONS

In order to obtain information regarding the nature of the NiPt phase stability, we performed a neutron experiment on a "null-matrix" single crystal to measure the separate occupational probabilities (correlations) given by the SRO parameters and related to the EPIs, and the SE parameters whose values will provide us, with one additional experiment, the individual pair-wise displacements of the atomic species from their average distances given by the lattice parameter.

The scans show only SE and SRO scattering with tiny Bragg peaks due to a very slight concentration mismatch, which were used to align the sample, but with no contribution from the TDS or HDS.

The SRO parameters, which are related to the concentration-correlation functions, indicate an ordering tendency similar to the low temperature $L1_0$ phase. The SE parameters, which depend on the concentration-displacement correlations, give us linear combinations of the species-dependent displacements for each shell. Individual displacement values will be obtained from our x-ray study. Nevertheless, considering that the size of the atoms dominates the ordering tendency we find that for first neighbors the Pt-Pt displacement, which is assumed to be positive (with the Ni-Ni displacement negative), is greater than 1.25% of the magnitude of the average nearest neighbor distance and the Ni-Pt displacement is almost certainly negative.

Pinski *et al.*[8] found that the electronic states induced by size disparity and due to bandwidth differences (related to off-diagonal disorder in tight-binding theory), are essentially responsible for ordering, while electronegativity does not play a role; notably, spin-orbit coupling contributes nothing due to its relative magnitude. For completeness, the tight-binding methods describe the size-induced strain interactions as off-diagonal disorder, but do not contain the hybridization (hence correct off-diagonal disorder) that occurs in many systems, and thus obscures the physics; such hybridization is missing because it is not obtained from any usual method to get effective off-diagonal parameters taken from the elements, such as their average or geometric mean, but can be obtained from first-principles calculated phase shifts.[52]

The normal crystal shows essentially zero neutron contrast for SRO and SE scattering, but very clear HDS in preferential directions. The HDS analysis using these data remains to be performed. In the present null-matrix experiment, using the KCM and GEM theories, we obtained EPIs with essentially no difference between the two methods, because the concentration is nearly 50%, showing considerable interactions mainly for the first four neighbors; the rest decay rapidly to zero. The ratios of $V(2)/V(1)=-0.2$ and $V(3)/V(1)=0.06$ agree with the ordered ground state structure predicted by Clapp and Moss[33] for a fcc crystal, where the minima of $V(\mathbf{q})$ occur at (100) and equivalent points. A numerical comparison of these results, both with electronic structure theory and computational simulations, should yield considerable information on the NiPt phase stability problem, especially after our companion x-ray experiment is concluded.

ACKNOWLEDGMENTS

We thank B. J. Wuensch for providing the absorption correction algorithm for an arbitrary crystal shape and D. D. Johnson for helpful discussion of the theoretical calculations. This work was supported in Houston in part by the National Science Foundation under Contract No. DMR-0099573. We acknowledge the support of the National Institute of Standards and Technology, U.S. Department of Commerce, in providing the neutron research facilities used in this work. This work utilized facilities supported in part by the National Science Foundation under Grant No. DMR-0454672. The work at Oak Ridge was supported in part under the auspices of the U.S. Department of Energy. The HFIR Center for Neutron Scattering is a national user facility funded by the U.S. Department of Energy, Office of Basic Energy Sciences–Materials Science, under Contract No. DE-AC05-00OR22725 with UT-Battelle, LLC.

---

*Present addresses: Department of Materials Science and Engineering, University of Maryland, College Park, MD 20742-2115, USA and National Institute of Standards and Technology, 100 Bureau Drive, MS 8562, Gaithersburg, MD 20899-8562, USA.

[1] V. Heine and J. Sampson, J. Physiol. (London) **13**, 2155 (1983).
[2] A. Bieber and F. Gauthier, Acta Metall. **34**, 2291 (1986).
[3] W. Hume-Rothery, *Electrons, Atoms, Metals and Alloys* (Dover, New York, 1963).
[4] Y. Gauthier, Y. Joly, R. Baudoing, and J. Rundgren, Phys. Rev. B **31**, 6216 (1985).
[5] R. Baudoing, Y. Gauthier, M. Lundberg, and J. Rundgren, J. Phys. C **19**, 2825 (1986).
[6] G. Treglia and F. Ducastelle, J. Phys. F: Met. Phys. **17**, 1935 (1987).
[7] G. M. Stocks, W. M. Temmerman, and B. L. Gyorffy, Phys. Rev. Lett. **41**, 339 (1978).
[8] F. J. Pinski, B. Ginatempo, D. D. Johnson, J. B. Staunton, G. M. Stocks, and B. Gyorffy, Phys. Rev. Lett. **66**, 766 (1991).
[9] Z. W. Lu, S.-H. Wei, A. Zunger, S. Frota-Pessoa, and L. G. Ferreira, Phys. Rev. B **44**, 512 (1991).
[10] N. Takeuchi, C. T. Chang, and K. Ho, Phys. Rev. Lett. **63**, 1273 (1989).
[11] V. Fiorentini, M. Methfessel, and M. Scheffler, Phys. Rev. Lett. **71**, 1051 (1993).
[12] R. H. M. Smit, Phys. Rev. Lett. **87**, 266101 (2001).
[13] L. G. Wang and A. Zunger, Phys. Rev. B **67**, 092103 (2003).
[14] V. N. Bugaev, H. Reichert, O. Shchyglo, O. Udyansky, Y. Sikula, and H. Dosch, Phys. Rev. B **65**, 180203(R) (2002).
[15] S. Dietrich and W. Fenzl, Phys. Rev. B **39**, 8873 (1989a).
[16] S. Dietrich and W. Fenzl, Phys. Rev. B **39**, 8900 (1989b).
[17] L. Reinhard, J. L. Robertson, S. C. Moss, G. E. Ice, P. Zschack, and C. J. Sparks, Phys. Rev. B **45**, 2662 (1992).
[18] B. Mozer, D. T. Keating, and S. C. Moss, Phys. Rev. **175**, 868 (1968).
[19] J. Vrijen and S. Radelaar, Phys. Rev. B **17**, 409 (1978).
[20] W. Wagner, R. Poerschke, A. Axmann, and D. Schwahn, Phys. Rev. B **21**, 3087 (1980).
[21] J. M. Cowley, J. Appl. Phys. **21**, 24 (1950).
[22] B. E. Warren, *X-ray Diffraction* (Dover, New York, 1990).
[23] B. E. Warren, B. L. Averbach, and B. W. Roberts, J. Appl. Phys. **22**, 1493 (1951).
[24] W. Schweika, *Disordered Alloys: Diffuse Scattering and Monte*

Carlo Simulations, Springer Tracts in Modern Physics Vol. 141 (Springer-Verlag, Berlin, Germany, 1988).

[25] B. Schoenfeld, *Local Atomic Arrangements in Binary Alloys* (Institut fuer Angewandte Physik, ETH Zurich-Habilitations Schrift, 1993).

[26] G. E. Ice, J. L. Robertson, and C. J. Sparks, in *Methods in Materials Research: A Current Protocals Publication*, edited by E. N. Kaufmann and A. Goldman (John Wiley and Sons, New York, 1998).

[27] T. R. Welberry and B. D. Butler, J. Appl. Crystallogr. **41**, 591 (1985).

[28] B. Borie, Acta Crystallogr. **10**, 89 (1957).

[29] B. Borie, Acta Crystallogr. **12**, 280 (1959).

[30] C. B. Walker and D. T. Keating, Acta Crystallogr. **14**, 1170 (1961).

[31] M. A. Krivoglaz, *Theory of X-Ray and Thermal Neutron Scattering by Real Crystals* (Plenum, New York, 1969); M. A. Krivoglaz, *X-Ray and Neutron Diffraction in Nonideal Crystals* (Springer, Berlin, 1995); M. A. Krivoglaz, *Diffuse Scattering of X-rays and Neutrons by Fluctuations* (Springer, Berlin, 1996).

[32] P. C. Clapp and S. C. Moss, Phys. Rev. **142**, 418 (1966).

[33] P. C. Clapp and S. C. Moss, Phys. Rev. **171**, 754 (1968).

[34] S. C. Moss and P. C. Clapp, Phys. Rev. **171**, 764 (1968).

[35] L. Reinhard and S. C. Moss, Ultramicroscopy **52**, 223 (1993).

[36] P. A. Flinn, Phys. Rev. **104**, 350 (1956).

[37] W. Schweika and H. G. Haubold, Phys. Rev. B **37**, 9240 (1988).

[38] V. Gerold and J. Kern, Acta Metall. **35**, 393 (1987).

[39] P. C. Gehlen and J. B. Cohen, Phys. Rev. **139**, A844 (1965).

[40] I. V. Masanskii, V. I. Tokar, and T. A. Grishchenko, Phys. Rev. B **44**, 4647 (1991).

[41] B. W. Roberts, Acta Metall. **2**, 597 (1954).

[42] J. R. D. Copley and J. C. Cook, Chem. Phys. **292**, 447 (2003).

[43] J. R. D. Copley, *The Disk Chopper Spectrometer at NIST: The Good, the Bad and the Ugly*, Proceedings of the 17th International Collaboration on Advanced Neutron Sources (Los Alamos National Laboratory, LA-UR 06-3904, 2006), Vol. III, p. 974.

[44] W. H. Press, S. A. Teukolsky, W. T. Vetterling, and B. P. Flannery, *Numerical Recipes in C* (Cambridge University Press, Cambridge, UK, 1999).

[45] B. Borie, Acta Crystallogr. **14**, 472 (1961).

[46] H. Reichert, A. Schops, I. B. Ramsteiner, V. N. Bugaev, O. Shchyglo, A. Udyansky, H. Dosch, M. Asta, R. Drautz, and V. Honkimaki, Phys. Rev. Lett. **95**, 235703 (2005).

[47] Z. W. Lu, S.-H. Wei, and A. Zunger, Phys. Rev. Lett. **68**, 1961 (1992).

[48] F. J. Pinski, B. Ginatempo, D. D. Johnson, J. B. Staunton, G. M. Stocks, and B. L. Gyorffy, Phys. Rev. Lett. **68**, 1962 (1992).

[49] K. Huang, Proc. R. Soc. London **190**, 102 (1947).

[50] P. H. Dederichs, J. Phys. F: Met. Phys. **3**, 471 (1973).

[51] R. W. James, *Optical Principles of the Diffraction of X-rays* (G. Bell and Sons, London, UK, 1949).

[52] D. D. Johnson (private communication).